ACS NANO

www.acsnano.org

ARTICLE

Room-Temperature Lasing at Flatband Bound States in the Continuum

Thi Thu Ha Do,[▽] Zhiyi Yuan,[▽] Emek G. Durmusoglu, Hadi K. Shamkhi, Vytautas Valuckas, Chunyu Zhao, Arseniy I. Kuznetsov, Hilmi Volkan Demir, Cuong Dang, Hai Son Nguyen,* and Son Tung Ha*

Cite This: *ACS Nano* 2025, 19, 19287−19296

Read Online

ACCESS | Metrics & More | Article Recommendations | Supporting Information

ABSTRACT: **High-quality factor optical modes with a low dispersion in the momentum space are highly desirable for applications such as low-threshold lasers, strong light−matter interactions, and optical trapping. Bound states in the continuum (BICs) have recently gained attention as a promising optical cavity concept due to their theoretically infinite quality factors. However, their quality factor decreases exponentially when deviating from the BIC singularity in the momentum space, which limits their practical use. Here, we present a design concept and experimental realization of flatband BICs in a rectangular array of titanium dioxide nanopillars. By precisely engineering the interaction between four counterpropagating guided modes in the array, a nondispersive BIC band can be obtained. The flatband BIC exhibits an enhanced quality factor near the Γ-point by 2 orders of magnitude compared to that of the symmetry-protected BIC mode in a square array, along with an exceptionally high optical density of states. As a result, we achieve room-temperature lasing at the flatband BIC with a quality factor of ∼9100 and a threshold 4 times lower than that of the symmetry-protected BIC. The flatband-BIC lasing properties, such as directionality and topological charge, are also studied in detail. The concept and outstanding lasing performance of the flatband BICs presented in our work mark an important step toward efficient optical cavities and microlasers and hold great potential for advanced photonic and optoelectronic devices.**

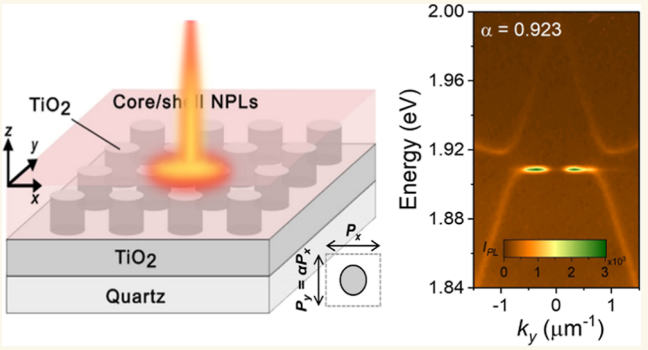

KEYWORDS: *flatband, bound states in the continuum, super-BIC, room-temperature lasing, nanoplatelets, 2D nanomaterials*

Improving the quality of optical cavities has been the central focus and is of continuously growing interest due to their vital roles in various research fields such as optics, polaritonics, and quantum computing. The quality factor (*Q*-factor), which describes the energy loss rate, is the key metric for assessing the effectiveness of an optical cavity in nanophotonic devices. Significant progress has been made in high-*Q* cavities over the past decades, particularly in defect-based photonic crystals. While these structures offer exceptional field localization and *Q*-factor up to ∼10^6, they are highly sensitive to structural disorders, as extensively discussed in refs 1 and 2 and references therein.

Bound states in the continuum (BICs), first predicted mathematically by Wigner and von Neuman in 1929,[3] are distinctive modes because they remain completely decoupled and, therefore, nonradiative despite lying within the continuous radiative spectrum of the extended states.[4] In nonlocal metasurfaces such as photonic crystal slabs or periodic subwavelength lattices, BICs are Bloch resonances that exhibit extremely high *Q*-factors ($Q_{BIC} \rightarrow \infty$ in theory) and manifest themselves as singularities of polarization vortices in the far-field radiation. Such unique properties of BICs have been extensively exploited for microlasers,[5−9] optical sensors,[10−12] strong light−matter interactions,[13−17] and nonlinear phenomena.[18−21] The confinement of BIC modes in photonic metasurfaces originates either from the symmetry-mismatch for symmetry-protected BICs located at high-symmetry points of the Brillouin zone or from the destructive interference between leaky resonances for Friedrich−Wintgen BICs located at arbitrary points in the momentum space.[4,22] Nevertheless,

Received: February 3, 2025
Revised: April 30, 2025
Accepted: April 30, 2025
Published: May 12, 2025

BIC cavities face an inherent limitation of the fast attenuating Q-factors as moving away from the BIC conditions ($Q \sim 1/(k - k_{BIC})^2$, where k denotes the wavevector) primarily due to the radiative losses of neighboring resonances that hinder the practicability of BIC cavities in wide-angle applications. Taking advantages of the unique topological nature of BICs,[23] merging multiple BICs in the momentum space to form super-BICs has been demonstrated to alter the scaling rule and, subsequently, Q-factors of nearby states can be significantly enhanced by orders of magnitude.[24−28]

Another important yet rarely discussed factor governing the performance of optical cavities is the band dispersion. Weakly dispersive or even dispersionless bands exhibit small group velocity and large density of states (DOS), which consequently amplify the interaction between photons and gain media and, hence, enhance the stimulated emission rate.[29,30] The scaling of the gain with group velocity and optical DOS is discussed in ref 31. Some typical examples of flatband modes such as Kagome, sawtooth, Lieb lattice, super-honeycomb lattice,[32,33] and Moiré lattice[34−36] have enabled various optical applications such as slow light,[29,37] distortion-free image transmission,[38] optical nonlinearities,[39,40] polariton condensation,[41] and reconfigurable coherent nanolaser arrays.[42] Moiré BICs have been theoretically proposed in bilayer photonic crystal slabs[39] that can enable band flatness. However, these proposed structures are challenging to fabricate as they require either high-precision two-step nanofabrication or manually stacking two metasurfaces with controllable interlayer air-gap. Very recently, by merging two grating layers into an one-dimensional slab, Moiré BICs have been experimentally realized showing a Moiré band with a Q-factor of ∼9042.[43] However, this approach faces a trade-off between band flatness and Q-factor, and it requires a sufficient number of tunable parameters to suppress all the diffraction channels.

In this work, we design and investigate a novel concept of flatband BICs, which exploit both a high Q-factor over a wide range of wavevectors and exceptionally large density of states induced by the slow-dispersion of the flatband in the vicinity of the BIC singularity. Our strategy leverages the engineering of the photonic band curvature through the strong interaction between guided resonances in periodic metasurfaces, eliminating the need for BIC merging. By fine-tuning the anisotropy of a rectangular array of titanium dioxide (TiO_2) nanopillars, defined as a ratio between the periodicity along the y- and x-directions, we observe the transition of the band curvature from negative to positive. A flatband BIC is identified with a zero curvature, singularity of the Q-factor at Γ-point, and topological nature revealed by a polarization vortex in the momentum space. Additionally, at the flatband-BIC condition, we observe a substantial increase of the Q-factor by 2 orders of magnitude of the states near the Γ-point and a sharp increase of DOS compared to that of the symmetry-protected BICs. Our experimental results are supported by theoretical calculation including both numerical simulations and an analytical model. Moreover, we demonstrate a flatband-BIC laser operating at room temperature that shows a 4-fold reduction in the lasing threshold compared to standard symmetry-protected BICs in a square lattice. The implication of flatband BICs with a high Q-factor and large density of states can be extended beyond lasing to other applications such as sensing, polaritonic physics, optical trapping, and nonlinear optics.

RESULTS AND DISCUSSION

Concept and Design. Figure 1a illustrates a schematic of our photonic metasurface, featuring a rectangular periodic lattice of dielectric nanopillars made of high-refractive-index, lossless titanium dioxide (TiO_2, $n_{TiO_2} \sim 2.45$, $\kappa_{TiO_2} \sim 0$ at λ = 650 nm) on top of a TiO_2 slab, and a quartz substrate. The structure is coated with a $CdSe/Cd_xZn_{1-x}S$ core-alloyed shell nanoplatelet (NPLs) layer that serves as a gain medium. The period along the x-axis is set at p_x = 325 nm, whereas the y-axis period (p_y) is varied from 295 to 325 nm. The lattice anisotropy factor, defined as $\alpha = p_y/p_x$ in the real space, corresponds to the anisotropy in the reciprocal space ($\alpha = k_x/k_y$) and serves as the sole tunable parameter in this study. All simulation and experimental data presented in this manuscript are resolved along k_y and with transverse magnetic (TM) polarization (i.e., polarizer aligned along the y-axis), unless specified.

Figure 1b−e presents the photonic band structures of the nanopillar arrays along the Γ−Y direction (k_x = 0) for various anisotropic factors (α) calculated using the finite-element method (FEM) (COMSOL Multiphysics; see details in the Methods Section). Our analysis focuses on the evolution of two bands, identified as "lower band" (LB) and "upper band" (UB) in these figures. Particular attention is given to a high-Q mode at the Γ-point (symmetry-protected BIC or SP-BIC) and two high-Q modes located at oblique angles (Friedrich−Wintgen quasi-BIC or FW-qBIC). When α = 1.000 (i.e., a square lattice of nanopillars), both the SP-BIC and FW-qBICs are positioned on the upper band. With the introduction of the lattice anisotropy (i.e., α < 1), the FW-qBICs remain on the upper band but shift to higher wavevectors, while the SP-BIC is located at the Γ-point of the lower band. By varying α, the curvature (C) of the lower band near the Γ-point (i.e., ∼±1 μm^{-1}) can be tuned from negative (e.g., α = 0.963) to positive (e.g., α = 0.892) and reaches the flatband condition (C = 0) when $\alpha \approx 0.923$. The effective mass of photons coupled to the lower band can be calculated from the band curvature C as $m_y^* = \hbar^2/(d^2E/dk_y^2) = \hbar/C$. Figure 1f presents the evolution of the relative effective mass (m_y^*/m_e) versus α, where m_e is the free electron mass ($m_e = 9.1 \times 10^{-31}$ kg). The lower band becomes a flatband BIC (FB-BIC) in the array with an optimal lattice anisotropy value where the photon effective mass approaches infinity ($|m_y^*| \to \infty$).

To further understand the formation of the flatband BIC, we develop an analytical model based on the coupled mode theory (CMT) as detailed in Section SI of the Supporting Information. We consider the interaction between the four lowest-energy guided mode resonances with TM-like polarization: (+1, 0), (−1, 0) propagating along the x-direction and (0, +1), (0, −1) propagating along the y-direction (Figure S1, Supporting Information), to explain the emergence of different BIC modes (SP-BICs, FW-qBICs, FB-BIC) and the band transformation when tuning the anisotropic factor α. The interplay of diffractive and radiative coupling among these four guided modes determines the curvature and Q-factor of the bands. In particular, the hybridization of the negative-curvature states at off-Γ points and the positive-curvature SP-BIC state at the Γ-point, both on the lower band, leads to the formation of flatband BIC on the lower band and FW-qBIC on the upper band. Using our analytical model, we also calculate the effective masses and the photonic band structures for arrays with different lattice anisotropy, which agree well with

https://doi.org/10.1021/acsnano.5c01972
ACS Nano 2025, 19, 19287−19296

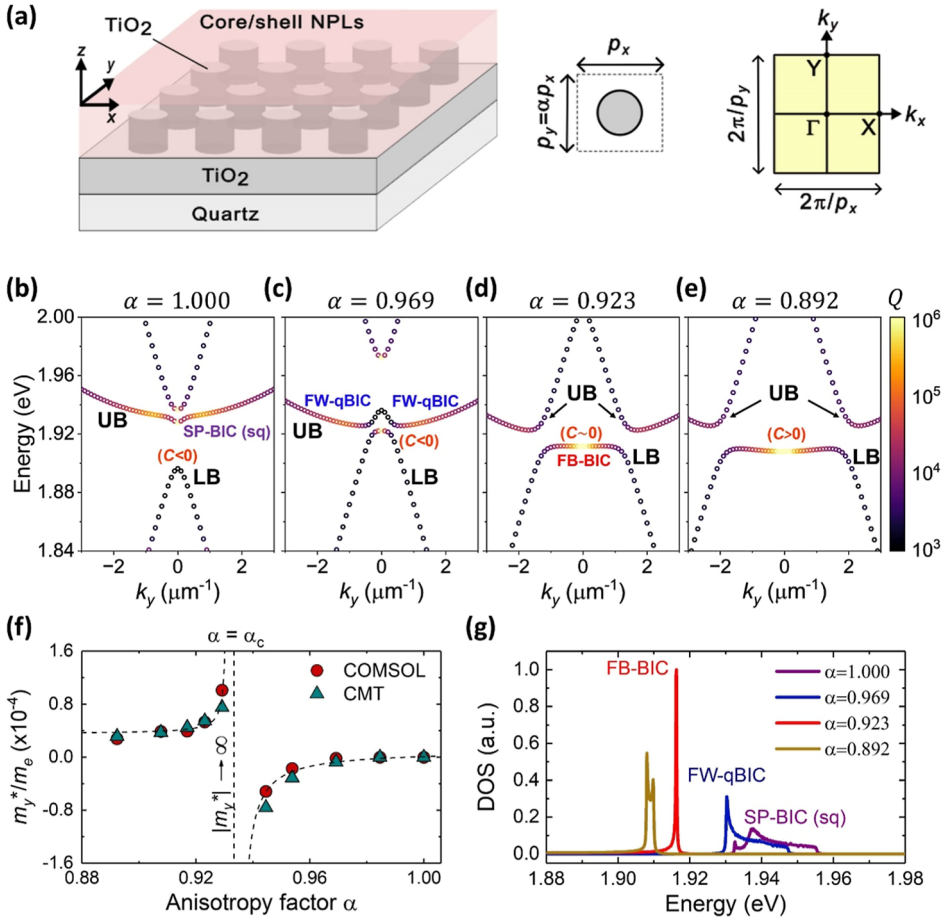

Figure 1. Design concepts and characteristics of flatband-BICs. (a) Schematic of the device structure consisting of TiO_2 nanopillars covered with core/shell NPLs on a TiO_2 slab on top of a quartz substrate. The nanopillar arrays have a rectangular unit cell with a varying anisotropy factor $\alpha = p_y/p_x$ (equivalently, $\alpha = k_x/k_y$ in the Brillouin zone). (b–e) Simulated band structure along the k_y-direction ($k_x = 0$) for TM-polarization showing the evolution of the curvature C of the lower band for $\alpha = 1.000$ ($C < 0$) in (b), $\alpha = 0.969$ ($C < 0$) in (c), $\alpha = 0.923$ ($C \sim 0$, flatband-BIC) in (d), and $\alpha = 0.892$ ($C > 0$) in (e). The color code indicates the Q-factor of all the bands. (f) Relative photon effective mass of the lower band at the Γ-point (k_x, $k_y = 0$) extracted from the band curvature C in COMSOL simulation (red circles) and coupled mode theory (blue triangles) showing excellent agreement and both revealing the transition from positive ($m_y^* > 0$) to negative curvature ($m_y^* < 0$) as α increases, with the FB-BIC occurring at $\alpha = \alpha_c$ when $C = 0$ or $|m_y^*| \to \infty$. The black dashed lines are guides for the eyes. (g) Density of states (DOS) plotted for $\alpha \sim 0.892$ (yellow-brown curve), $\alpha \sim 0.923$ (red curve), $\alpha \sim 0.969$ (blue curve), and $\alpha \sim 1.000$ (purple curve), showing the maximum DOS obtained at the FB-BIC condition ($\alpha \sim 0.923$) and the significant enhancement of ~3 and ~7 times compared to FW-qBIC and SP-BIC in a square lattice, respectively.

numerical simulations and the experimental results, as shown in Figures 1f and S2, respectively. Differently from the flatbands observed in special lattices, such as Kagome, Lieb, and Moiré lattices,[32−36] which remain nondispersive in the entire momentum space and tightly localized in real space, flatband BICs in our finely tuned metasurfaces exhibit the dispersionless properties within a finite momentum range around the BIC singularity, where the BIC-related applications can be effectively utilized.

In addition to observing the evolution of band curvature, we notice a significant change in the divergence of the Q-factor in k-space under anisotropic lattice conditions. In the square lattice, the Q-factor diverges at the Γ-point and decays fast with regard to k ($Q \sim 1/k_y^2$). As the lattice deviates from the square configuration, the Q-factor exhibits a slower decay rate. Notably, the Q-factors of the off-Γ states on the FB-BIC (i.e., $\alpha = \alpha_c$) are greater by 2 orders of magnitude than those of the standard SP-BIC in the square lattice (see Figure S3, Supporting Information).

Based on the calculated band dispersions and Q-factors, we derive the density of optical states of the lower band for four representative cases: $\alpha = 0.892$ (yellow-brown curve), $\alpha = 0.923$ (red curve), $\alpha = 0.969$ (blue curve), and $\alpha = 1.000$ (purple curve) as shown in Figure 1g (see Section SII, Supporting Information for detailed calculation). As a result of the unique dispersionless behavior and the high-Q characteristics, the FB-BIC exhibits the maximum DOS with a significant DOS enhancement of ~3 and ~7 times as compared to FW-qBIC and SP-BIC in the square lattice, respectively. Such enhanced DOS and the corresponding reduced group velocity particularly favors the lowering of lasing thresholds.[29−31]

Experimental Demonstration of Flatband BICs. The TiO_2 nanopillar arrays were fabricated by using electron beam lithography followed by inductively coupled plasma reactive ion etching and wet etching processes. All the arrays presented in this work have a pillar height of ~100 nm and a diameter of ~290 nm fabricated on top of a slab of the same material with a thickness of 100 nm. The typical scanning electron

https://doi.org/10.1021/acsnano.5c01972
ACS Nano 2025, 19, 19287−19296

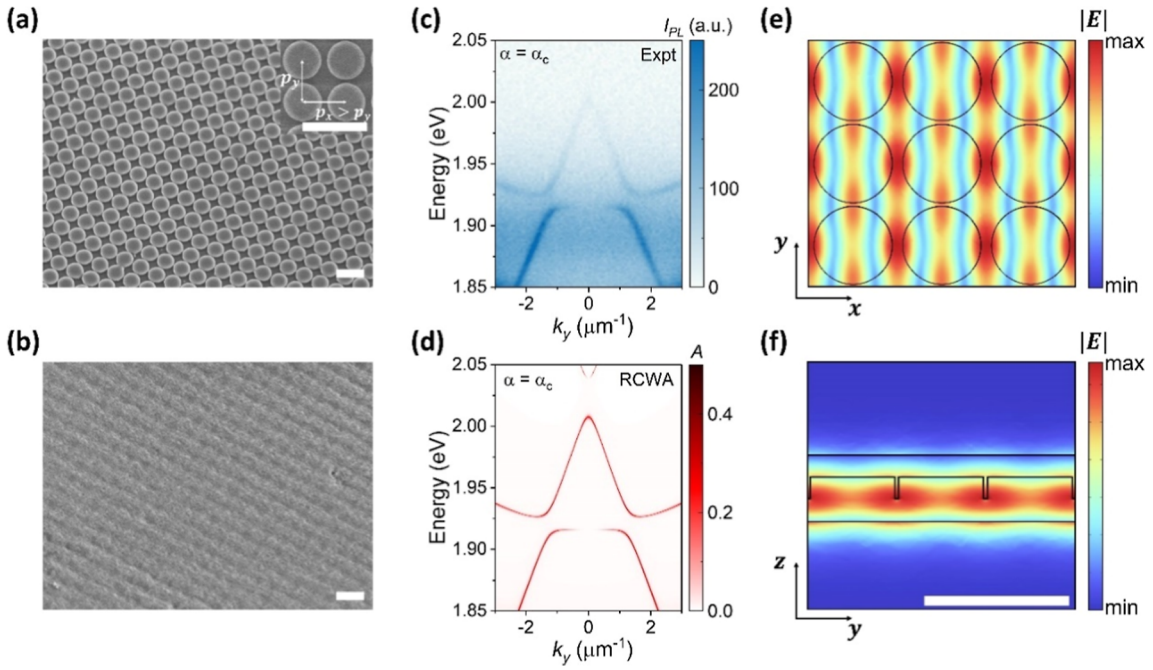

Figure 2. Structural and optical characterization of the flatband BIC. (a,b) Low-magnification scanning electron microscopy (SEM) image of a representative rectangular array of TiO_2 nanopillars after fabrication (a) (inset: high-magnification image zoomed in on a unit cell with $p_y < p_x$) and after being coated with nanoplatelets (b). (c) Experimental angle-resolved photoluminescence spectrum and (d) simulated angle-resolved absorption spectrum for the flatband-BIC case ($\alpha = \alpha_c$) resolved along the k_y-direction and TM-polarization obtained by RCWA simulation showing excellent agreement with the experimental data. Near-field distribution of the FB-BIC mode ($\alpha = \alpha_c$) in the (e) *xy*-plane and (f) *yz*-plane, showing the elongation of the electric field along the gap in the *y*-direction and the extension of the field to the top NPL layer. All the white scale bars represent 500 nm.

microscopy (SEM) images of the fabricated arrays are shown in Figure 2a.

The $CdSe/Cd_xZn_{1-x}S$ core-alloyed shell NPLs were synthesized by the hot injection method using four-monolayer CdSe core NPLs as seed nanocrystals[44] (see Methods Section and Section SIII, Figure S4, Supporting Information, for the architectural concept and characterization of NPLs). High-resolution transmission electron microscopy (HRTEM) reveals the square-shaped NPLs and the homogeneous size distribution (see Figure S4b,c, Supporting Information). The core-alloyed shell NPLs exhibit two exciton absorption peaks at ~1.92 eV and ~2.12 eV originating from the light-hole and heavy-hole transitions, respectively, and a strong photoluminescence (PL) at ~1.90 eV with a narrow full-width at half-maximum (fwhm) of ~60 meV (see Figure S4d, Supporting Information). For film processing, the core-alloyed shell NPLs are concentrated in an octane−hexane mixture and deposited onto the TiO_2 nanopillar array via spin-coating. The NPLs fill in the voids between TiO_2 nanopillars as shown in Figure 2b.

The optical properties were investigated using a home-built angle-resolved microspectroscopy setup (see Methods Section). A nanosecond-pulsed laser operating at λ_{exc} = 532 nm was focused onto the sample with a spot diameter of ~50 μm, equal to the size of the fabricated arrays. The photoluminescence (PL) emission from the sample was collected by a microscope objective, guided through a lens system that allows to image the back focal plane of the objective onto the entrance slit of the spectrometer. A pair of a half-waveplate and a linear polarizer (analyzer) was used to separate different polarization components of the optical signals. Figure 2c shows measured angle-resolved PL spectra along k_y with TM-polarization for the array with an optimal p_y/p_x ratio (i.e., $\alpha = \alpha_c = 0.923$). A complete set of angle-resolved PL measurements with different configurations for this array is shown in Figure S5, Supporting Information.

Figure 2d shows the simulated angle-resolved absorption spectrum by rigorous coupled-wave analysis (RCWA) for the array with FB-BIC ($\alpha = \alpha_c$), showing excellent agreement with the experimental angle-resolved PL spectra described above. Comparison between experimental measurements and RCWA simulations for arrays with different α are shown in Figure S6, Supporting Information. These results are consistent with the calculated band structures by COMSOL numerical analysis in Figure 1 and our CMT model in Figure S2.

The formation of flatband BIC with the enhanced *Q*-factor over an extended range in the momentum space described in our work is mediated by the strong coupling between photonic bands that alters both real and imaginary parts of the optical modes. The FW-qBICs and SP-BIC lie on two different bands. The physical mechanism here is clearly distinct from the super-BIC obtained from merging multiple BICs with different topological charges on the same band, where only the imaginary part is controlled.[24−26] Furthermore, due to the same parity of the interacting guided modes, our design is independent of vertical symmetry, whereas a broken symmetry is required for band hybridization in the grating structure.[28,45,46] Engineering the curvature and *Q*-factor dispersion of BIC bands via band coupling is a versatile strategy that can create several flatband BICs with different energies in a single design (see Figure S7, Supporting Information), suggesting the potential for multiwavelength applications such as multi-wavelength lasing or multiplexed sensing.

https://doi.org/10.1021/acsnano.5c01972
ACS Nano 2025, 19, 19287−19296

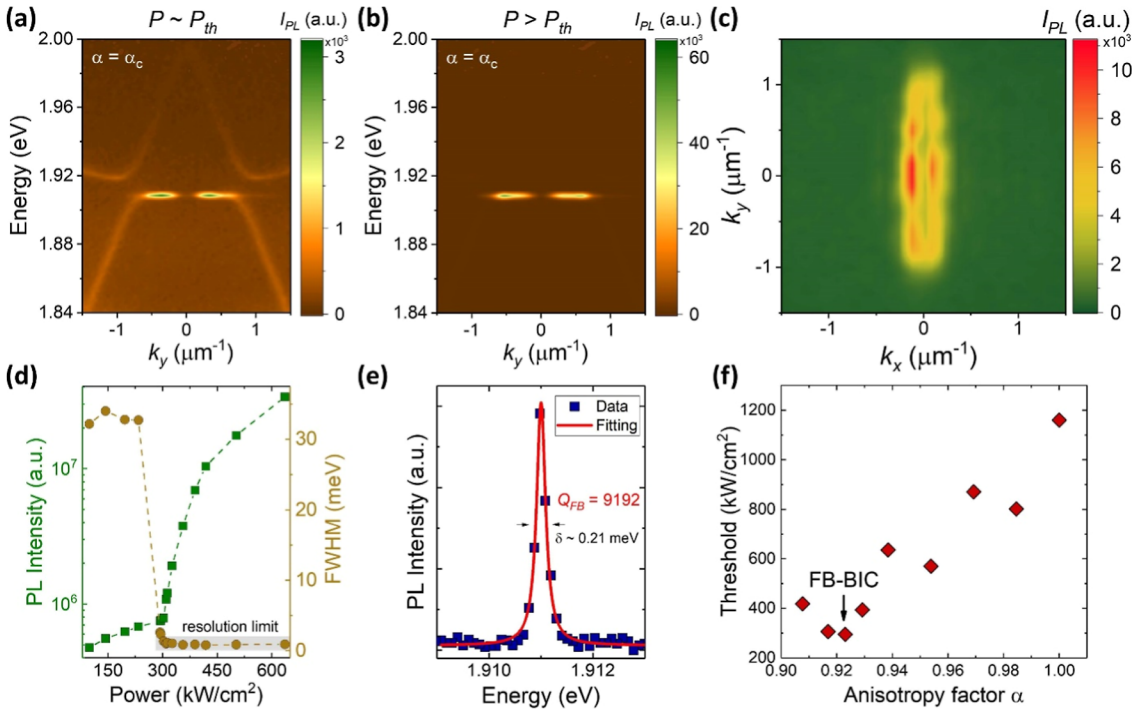

Figure 3. Characterizations of the flatband-BIC laser. (a,b) Angle-resolved photoluminescence spectra taken for the case of FB-BIC ($\alpha = \alpha_c$) at (a) near ($P \sim P_{th}$) and (b) above the lasing threshold ($P > P_{th}$). (c) Back focal plane image of the lasing emission for FB-BIC. (d) Typical PL intensity versus excitation power in a semilog scale and the full width at half-maximum (fwhm) versus excitation power, analyzed over the PL spectral range from 1.77 to 2.07 eV, showing the superlinear increase of the PL intensity and the reduction of the fwhm after the lasing threshold of ~295 kW/cm^2. (e) High-resolution lasing spectrum at the FB-BIC mode, showing the highest lasing Q-factor of ~9192. (f) Lasing threshold as a function of lattice anisotropy factor α, showing the lowest threshold obtained at the FB-BIC condition α = 0.923, which is ~4 times lower than that of the standard SP-BIC (α = 1.000).

Figure 2e,f displays the simulated near-field distributions associated with the flatband-BIC mode ($\alpha = \alpha_c$) in the nanocylinders along xy- (e) and yz-planes (f). The field extends into the gaps between pillars and ~50 nm into the NPLs layer on top of the pillars, ensuring a good overlapping of the optical mode with the gain medium. Compared to TM modes in a regular SP-BIC in a square lattice (Figure S8, Supporting Information), the electric field of the FB-BIC mode is elongated along the y-direction, reflecting the anisotropy of the lattice.

Efficient Microlaser Based on the Flatband-BIC Concept. An immediate application of the high-Q FB-BIC cavities is (but not limited to) microlasers. In this work, we choose core-alloyed shell NPLs as a gain medium for lasing because of their near-unity photoluminescence quantum yield (PLQY) of ~98.5% at room temperature, higher gain cross-section and stability compared to the only core NPLs.[44,47] The quantum confinement and, subsequently, the PL emission of the NPLs can be precisely controlled on demand via the shell growth reaction. In addition, an alloyed interface was engineered to reduce the lattice mismatch between the core and shell and to suppress Auger recombination, resulting in near unity PLQY.[47]

To achieve lasing, we excited the sample using a nanosecond laser emitting at 532 nm with a repetition rate of 1 kHz and a pulse duration of 1.5 ns at ambient conditions. Figure 3a shows the angle-resolved PL spectra of the flatband BIC ($\alpha = \alpha_c$) near the lasing threshold ($P \sim P_{th}$). We observe, on top of the background showing the lower band and the upper band, the strongly enhanced emission intensity at ~1.91 eV corresponding to the lasing occurring at the flatband BIC. When the pumping power is above the lasing threshold, the intensity increases rapidly and eventually dominates the whole emission spectra as shown in Figure 3b. The unpolarized lasing pattern of the flatband-BIC mode in the momentum space (k_x, k_y) is shown in Figure 3c. The lasing beams are confined along the k_x direction and elongated along the k_y direction following the dispersion of the flatband BIC along k_y.

As α changes, the Q-factor and DOS of the FW-qBICs at oblique angles rise and compete with the SP-BIC on the lower band. As a result, at α = 0.969, lasing occurs at the FW-qBICs. For the square lattice (α = 1.000), the SP-BIC jumps to the upper band and dominates (Figure S9, Supporting Information). The lasing pattern at FW-qBIC shows up along the k_y-direction with the intensity peaking at $|k_y| \sim 0.5\ \mu m^{-1}$ and diffusing to the nearby states at higher k_y, whereas for the standard square lattice, we observe four lobes in both x- and y-directions as the signature of the magnetic quadrupole mode that is clearly distinctive from the FB-BIC laser.

The lasing action in all cases was confirmed by performing spectral analysis of the integrated PL spectra over all emission angles at different pumping powers (see Figure S10, Supporting Information). Typical nonlinear S-curves of the output−input power dependence with a clear threshold and the narrowing line width (see Figures 3d and S11, Supporting Information) indicate the transition from the spontaneous to the stimulated emission regime, where the lasing threshold is determined to be ~295 kW/cm^2 for the case of FB-BIC. Noticeably, above the lasing threshold, the fwhm reduces to ~0.21 meV, revealing the ultrahigh Q-factor of up to ~9192 for the FB-BIC laser (see Figure 3e), which is higher than that of the standard SP-BIC lasing ($Q \sim 7062$, see Figure S12,

https://doi.org/10.1021/acsnano.5c01972
ACS Nano 2025, 19, 19287−19296

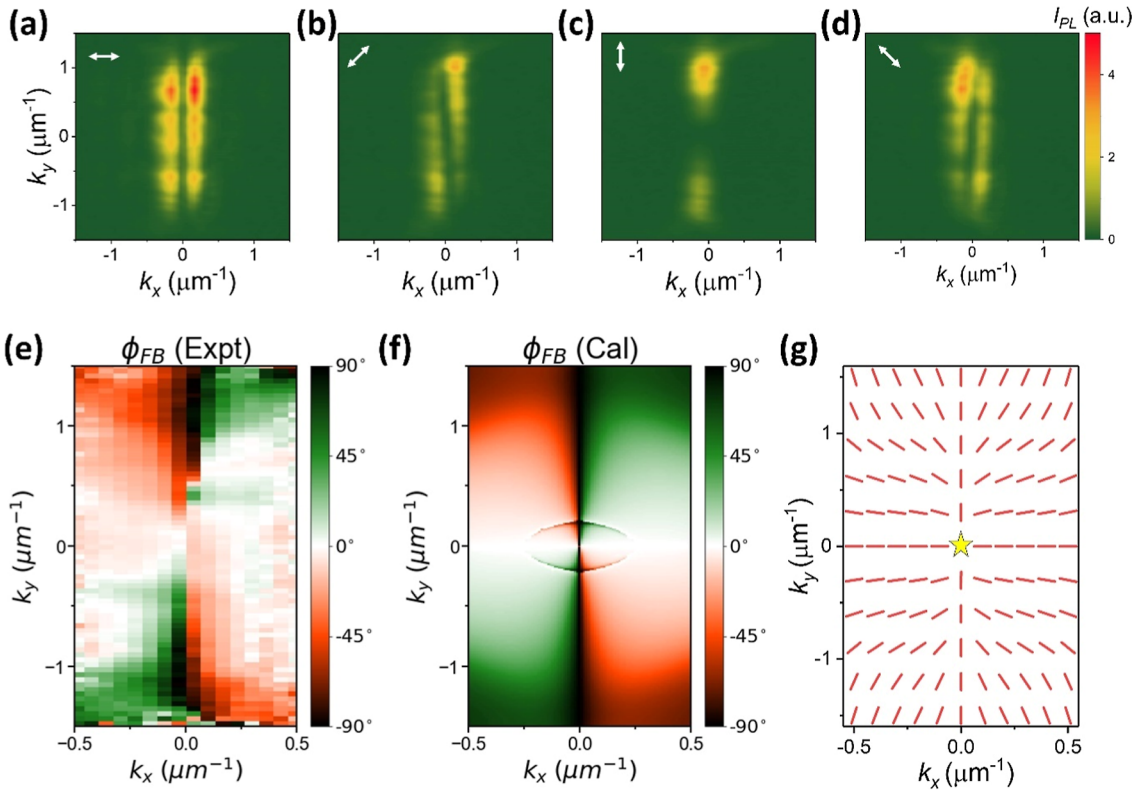

Figure 4. Topological properties of the flatband BIC. (a−d) Far-field lasing emission patterns of the FB-BIC measured in (a) horizontal, (b) diagonal, (c) vertical, and (d) antidiagonal direction plotted with the same scale bar. (e,f) Polarization mapping ϕ_{FB} of the experimental (e) and simulated (f) lasing emission. (g) Extracted polarization vectors around the FB-BIC singularity marked with a star, revealing the topological charge of +1 of the FB-BIC.

Supporting Information) and is among the highest Q reported in literature for BIC lasing. The switching of lasing among different modes while sweeping α is also observed in another set of arrays with pillar diameter $D \sim 285$ nm and $p_x = 320$ nm (see Figure S13).

Although lasing has been achieved for all devices, the lowest lasing threshold is obtained for the case of flatband BIC at $\alpha = \alpha_c$ (see Figure 3f). The threshold increases slightly for $\alpha < \alpha_c$, while it increases significantly for $\alpha > \alpha_c$. We find that the critical condition for flatband BIC mainly depends on the anisotropy factor of the metasurface lattice and is independent of the pillar size. Importantly, compared with the standard SP-BIC cavity, the threshold of the FB-BIC laser is reduced by ~4 times. This 4-fold reduction of the lasing threshold by using the FB-BIC cavity is comparable to that obtained by using super-BIC cavities after merging 9 single BICs.[26] The merging BICs approach is restricted to perfect vertical symmetry, while the FB-BIC created by our approach is independent of the vertical symmetry that makes the FB-BIC concept more robust for different optical systems. Thus, FB-BIC cavities can be designed and integrated into more complex on-chip devices, where many layers of different materials are present.[9] In this work, we focus on the design concept of the FB-BIC cavities and their effectiveness in lowering the lasing threshold of the standard SP-BIC lasers. We note that the absolute value of the lasing threshold in our FB-BIC laser device is not optimized. There are several strategies to further advance the performance of FB-BIC lasers, including, for instance, increasing the overlapping between gain media and photonic modes by either fabricating metasurfaces directly from stable high-index materials using III−V semiconductors, converting to the hole nanostructures filled with active materials such as quantum-wells or quantum dots, or further developing active materials with superior gain properties. For example, lead halide perovskite microstructures have recently been reported as excellent gain media with the record high optical gain value of up to 5077 cm^{-1}.[48] Additionally, coupling FB-BIC with strongly excitonic materials to form polaritons, where polariton lasing typically requires a much lower threshold, is another potential route.

Topological Properties of Flatband BIC. Furthermore, we explore the topological nature of the FB-BIC through the far-field polarization patterns in the momentum space, where BICs manifest themselves as singularities in the polarization map.[13,14,23,49,50] The measurements were performed at pumping powers above the lasing threshold to specifically select the signals only from the BIC modes of interest and follow the rotation of polarization states.

The topological charges q of BICs can be determined by the winding number of the polarization vector along a closed loop $\mathbf{C}'$ going in an anticlockwise direction around the BIC vortex as following[23]

$$q = \frac{1}{2\pi}\oint_{\mathbf{C}'} \mathrm{d}\boldsymbol{k}\cdot\nabla_{\boldsymbol{k}}\phi(\boldsymbol{k})$$

where $\phi(\boldsymbol{k})$ is the azimuthal angle of the linear polarization vector. In experiments, $\phi(\boldsymbol{k})$ can be calculated from Stokes parameters $S_1(\boldsymbol{k})$ and $S_2(\boldsymbol{k})$ as $\tan 2\phi(\boldsymbol{k}) = S_2(\boldsymbol{k})/S_1(\boldsymbol{k})$, where $S_1(\boldsymbol{k})$ and $S_2(\boldsymbol{k})$ are calculated from the far-field lasing patterns at different polarization configurations: horizontal, vertical, diagonal, and antidiagonal (see Figure 4a−d).[14] Since our BIC

https://doi.org/10.1021/acsnano.5c01972
ACS Nano 2025, 19, 19287−19296

bands are linearly polarized, $S_3(\boldsymbol{k})$ is negligible, and the ellipticity is approximately 0.

Figure 4e shows the experimental $\phi(\boldsymbol{k})$ map of the FB-BIC ($\alpha = \alpha_c$) that is clearly distinct from that of the standard SP-BIC (see Figure S14, Supporting Information). The Stokes parameters (see Figure S15, Supporting Information) and, subsequently, the polarization pattern of the FB-BIC mode are well reproduced in our simulation shown in Figure 4f. The extracted polarization texture is presented in Figure 4g showing the BIC vortex marked with a star. Encircling the FB-BIC singularity at $(k_x, k_y) = (0, 0)$ along the anticlockwise direction, the polarization evolves a full $+2\pi$ rotation, indicating the topological charge of +1 for the flatband BIC.

CONCLUSION

Our work presents the theoretical design and provides direct experimental evidence for flatband bound states in the continuum cavities, which exhibit a high quality factor with slow decay in the momentum space and can be obtained by merely tuning the anisotropy of the metasurface lattice. We demonstrate the significant enhancement of Q-factors of larger-k states nearby the BIC singularity by up to 2 orders of magnitude and the increase of density of states by 7 times compared to the symmetry-protected BIC in a symmetric square lattice that, in turn, leads to the reduction of the lasing threshold by 4 times in the flatband BIC. This advancement holds great potential for miniaturization of optical amplifiers and lasers, which are crucial components in integrated photonic chips. In addition, realizing flatband BICs also opens new opportunities for wide-angle, single-frequency applications and strong light−matter interactions.

METHODS SECTION

Fabrication of TiO_2 Nanostructures. The samples were fabricated using a quartz substrate coated with a 200 nm-thick titanium dioxide (TiO_2) film and a 20 nm-thick chromium (Cr) film by ion-assisted deposition (Oxford Optofab3000) and electron-beam evaporation (Angstrom EvoVac) techniques, respectively. Subsequently, hydrogen silsesquioxane (HSQ, Dow Corning), a negative electron beam resist, was deposited onto the TiO_2/Cr/quartz heterostructure via spin-coating at 5000 rpm for 60 s resulting in an ∼130 nm thick HSQ layer. The sample underwent a two-step baking process at 120 °C for 2 min and at 180 °C for 2 min subsequently. Electron beam lithography (Elionix ELS 7000) was performed at 100 keV to pattern the nanoantenna structures, followed by a development process in a salty developer (i.e., solution of 1 wt % NaOH and 4 wt % NaCl in deionized water)[51] for 4 min and rinsing with deionized water. The HSQ pattern was transferred to the Cr layer using inductively coupled plasma reactive ion etching (ICP-RIE, Oxford Plasmalab 100). The etching gas consisted of a mixture of chlorine (Cl_2) gas at 12 standard cubic centimeters per minute (sccm) and oxygen (O_2) gas at 2 sccm operating at a pressure of 10 mTorr and a temperature of 8 °C. The Cr pattern was then transferred to the TiO_2 layer by using trifluoromethane (CHF_3) gas flowing at the rate of 19 sccm with a pressure of 28 mTorr and a temperature of 20 °C. The etching time was calibrated such that only a 100 nm thick TiO_2 film was etched. Finally, the top HSQ and Cr masks were removed by immersing the whole sample in the Cr etchant solution (Merck) for 20 min, followed by rinsing in deionized water and blow-drying with nitrogen gas.

Synthesis of Nanoplatelets. *Chemicals.* Cadmium acetate dihydrate [$Cd(OAc)_2{\cdot}2H_2O$] (>98%), zinc acetate [$Zn(OAc)_2$] (99.99%), myristic acid (>99%), technical-grade 1-octadecene (ODE), selenium (Se) (99.99% all are trace metals basis), technical-grade oleic acid (OA) (90%), oleylamine (OLA) (70%), 1-octanethiol (≥98.5%), hexane, and ethanol (EtOH) were purchased from Sigma-Aldrich.

Synthesis of CdSe/$Cd_xZn_{1-x}S$ Core-Alloyed Shell NPLs. Synthesis of cadmium myristate and four-monolayer (4 ML) CdSe NPLs was performed following previously reported protocols.[52] For the synthesis of CdSe/$Cd_xZn_{x-1}S$ core-alloyed shell NPLs, we adapted a previous reported method.[44] 26.5 mg of $Cd(OAc)_2{\cdot}2H_2O$, 55 mg of $Zn(OAc)_2$, and 1 mL of OA in 5 mL of ODE were dried under vacuum at 80 °C for 60 min, followed by heating under argon at 200 °C for 10 min. After the solution was cooled to 80 °C, 1 mL of 4 ML of CdSe core NPL in hexane was added and degassed for another 30 min. Then the argon medium was restored, and the temperature was set to 300 °C. At 165 °C, 1 mL of OLA was swiftly injected, and 0.1 M octanethiol (in ODE) was injected with a rate of 10 mL/h using a syringe pump. When the temperature reached 300 °C, the solution was kept at this temperature until the targeted shell thickness was achieved, as confirmed by the emission peak at ∼650 nm. The NPL solution was cooled using a water bath. CdSe/$Cd_xZn_{x-1}S$ core-alloyed shell NPLs were purified by ethanol precipitation, followed by centrifugation at 6000 rpm. The precipitates were then redispersed in hexane.

Characterizations of NPLs. Absorbance and photoluminescence spectra of NPLs were recorded by using a Shimadzu UV-1800 and a Shimadzu RF-5301 PC spectrophotometer. The PLQY measurement setup was equipped with an Ocean Optics S4000 spectrometer and an integrating sphere. For the PLQY measurements, colloidal NPLs were excited at a wavelength of 405 nm (Cobolt Laser). The dimensions of core-alloyed shell NPLs were characterized by a JEOL TEM 2100F transmission electron microscope operated at 200 kV. A Woollam M-2000 spectroscopic ellipsometer, operating within the wavelength range 245−1690 nm, was employed to characterize the refractive index and the extinction coefficient of the NPLs. The ellipsometric parameters (Ψ and Δ) were fitted by using the B-spline model. NPL film thicknesses were measured by using a Bruker Dektak XT Step Profiler. The surface roughness of the NPL films was characterized by a Bruker Dimension XR Icon atomic force microscope.

Optical Characterizations. The optical properties of the samples were characterized by a home-built angle-resolved spectroscope using an inverted optical microscope (Nikon Ti-U). The optical signals were detected by a spectrometer (Andor SR-303i) consisting of a single grating with a groove density of 150 grooves/mm and an electron-multiplying charged-coupled detector (EMCCD, Andor Newton 971). For high-resolution spectra, a grating of 1200 grooves/mm was used.

The photoluminescence experiments were conducted using a pulsed laser operating at 532 nm with the pulse duration of 1.5 ns and the repetition rate of 1 kHz. The excitation beam was directed onto the sample surface via a top 10× microscope objective (NA = 0.3) with a spot diameter of ∼50 μm. The emission was collected through a 50× microscope objective (NA = 0.55). A suitable dichroic mirror was used to cut off the

https://doi.org/10.1021/acsnano.5c01972
ACS Nano 2025, 19, 19287−19296

532 nm laser line in the detection path. The entrance slit was opened completely (2500 μm width) for collecting the back focal image, while it was set to 50 μm for spectrally resolved angle-resolved photoluminescence or lasing spectra. For polarization-resolved measurements, a pair of a half waveplate and an analyzer was used along the detection path.

Numerical Simulations. The band structures, Q-factor, and density of states were simulated using COMSOL Multiphysics version 6.2. The angle-resolved absorption spectra were simulated using rigorous coupled-wave analysis (RCWA) in Lumerical with Bloch boundary conditions applied on the unit cell. The refractive indices of TiO_2 and NPLs were set as 2.45 and 1.8, respectively.

Coupled Mode Theory. Our analytical model considers a rectangular metasurface, characterized by two periods, p_x and $p_y = \alpha p_x$, where the anisotropic factor α is the only tuning variable. The interactions between photonic modes can be described by a non-Hermitian Hamiltonian H_f as $H_f = H_0 + H_c + H_{rad} + H_{non\text{-}rad}$, where H_0 is a diagonal matrix of lossless uncoupled modes, H_c represents the diffractive coupling term, and H_{rad} and $H_{non\text{-}rad}$ are non-Hermitian matrices representing the radiative coupling between the guided modes and the nonradiative losses, respectively. We consider the coupling between four lowest-energy folded guided modes $(n, m) = (+1, 0)$, $(-1, 0)$, $(0, +1)$, and $(0, -1)$, among which $(+1, 0)$, $(-1, 0)$ propagate along the x-direction and $(0, +1)$, $(0, -1)$ propagate along the y-direction. Details of the model and fitting parameters are discussed in detail in the Supporting Information, Section SI.

ASSOCIATED CONTENT

Supporting Information

The Supporting Information is available free of charge at https://pubs.acs.org/doi/10.1021/acsnano.5c01972.

Additional details for the analytical model, simulations, material characterizations, optical characterizations and numerical calculations for flatband BIC, and additional lasing data measured in different samples and under different conditions (PDF)

AUTHOR INFORMATION

Corresponding Authors

Hai Son Nguyen − *Ecole Centrale de Lyon, CNRS, INSA Lyon, CPE Lyon, INL, UMR 5270, Universite Claude Bernard Lyon 1, Ecully 69130, France; Institut Universitaire de France (IUF), Paris F-75231, France;* orcid.org/0000-0002-1638-2272; Email: hai-son.nguyen@ec-lyon.fr

Son Tung Ha − *Institute of Materials Research and Engineering, A*STAR (Agency for Science, Technology and Research), Singapore 138635, Singapore;* orcid.org/0000-0002-5475-8365; Email: ha_son_tung@imre.a-star.edu.sg

Authors

Thi Thu Ha Do − *Institute of Materials Research and Engineering, A*STAR (Agency for Science, Technology and Research), Singapore 138635, Singapore*

Zhiyi Yuan − *Institute of Materials Research and Engineering, A*STAR (Agency for Science, Technology and Research), Singapore 138635, Singapore; Centre for OptoElectronics and Biophotonics (COEB), School of Electrical and Electronic Engineering, Nanyang Technological University, Singapore 639798, Singapore; IRL 3288, CNRS-International-NTU-Thales Research Alliance (CINTRA), Singapore 637553, Singapore*

Emek G. Durmusoglu − *Luminous! Center of Excellence for Semiconductor Lighting and Displays, School of Electrical and Electronic Engineering, School of Physical and Mathematical Sciences, School of Materials Science and Engineering, Nanyang Technological University, Singapore 639798, Singapore;* orcid.org/0000-0001-6840-8342

Hadi K. Shamkhi − *Institute of Materials Research and Engineering, A*STAR (Agency for Science, Technology and Research), Singapore 138635, Singapore*

Vytautas Valuckas − *Institute of Materials Research and Engineering, A*STAR (Agency for Science, Technology and Research), Singapore 138635, Singapore*

Chunyu Zhao − *Luminous! Center of Excellence for Semiconductor Lighting and Displays, School of Electrical and Electronic Engineering, School of Physical and Mathematical Sciences, School of Materials Science and Engineering, Nanyang Technological University, Singapore 639798, Singapore*

Arseniy I. Kuznetsov − *Institute of Materials Research and Engineering, A*STAR (Agency for Science, Technology and Research), Singapore 138635, Singapore;* orcid.org/0000-0002-7622-8939

Hilmi Volkan Demir − *Luminous! Center of Excellence for Semiconductor Lighting and Displays, School of Electrical and Electronic Engineering, School of Physical and Mathematical Sciences, School of Materials Science and Engineering, Nanyang Technological University, Singapore 639798, Singapore; Department of Electrical and Electronics Engineering, Department of Physics, UNAM—Institute of Materials Science and Nanotechnology and National Nanotechnology Research Center, Bilkent University, Ankara 06800, Turkey;* orcid.org/0000-0003-1793-112X

Cuong Dang − *Centre for OptoElectronics and Biophotonics (COEB), School of Electrical and Electronic Engineering, Nanyang Technological University, Singapore 639798, Singapore; IRL 3288, CNRS-International-NTU-Thales Research Alliance (CINTRA), Singapore 637553, Singapore;* orcid.org/0000-0001-6183-4082

Complete contact information is available at: https://pubs.acs.org/10.1021/acsnano.5c01972

Author Contributions

[▽]T.T.H.D. and Z.Y. contributed equally to this work. S.T.H. and H.S.N. conceived the idea and started the project. T.T.H.D. fabricated the dielectric nanoantenna. Z.Y., H.K.S., and H.S.N. performed the theoretical simulations. H.V.D. and E.G.D. designed the core/shell nanoplatelet heterostructure and tailored it for coupling with the metasurface. E.G.D. synthesized and characterized the core/shell nanoplatelets and performed the deposition onto the metasurfaces. E.G.D. and C.Z. characterized the nanoplatelet films. V.V. characterized the metasurfaces. T.T.H.D. performed all the optical measurements and analyzed the experimental data. C.D., A.I.K., and H.V.D. discussed the data and the manuscript. T.T.H.D. wrote the manuscript with input from all the coauthors.

Notes

The authors declare no competing financial interest.

https://doi.org/10.1021/acsnano.5c01972
ACS Nano 2025, 19, 19287−19296

ACKNOWLEDGMENTS

T.T.H.D., H.K.S., V.V., A.I.K., and S.T.H. acknowledge the financial support from A*STAR MTC-Programmatic Fund (M21J9b0085). C.D. and Z.Y. acknowledge funding support from Singapore National Research Foundation Competitive Research Program (NRF-CRP29-2022-0003), Singapore Ministry of Education, under its AcRF Tier 1 grant (RG140/23). E.G.D., C.Z., and H.V.D. acknowledge the financial support from A*STAR MTC-Programmatic Fund (M21J9b0085) and the Ministry of Education, Singapore, under its Academic Research Fund Tier 1 (MOE-RG62/20), and from TUBITAK 121C266 and 20AG001. H.V.D. also acknowledges the support from TUBA and TUBITAK 2247-A National Leader Researchers Program (121C266). We also would like to acknowledge the Facility for Analysis, Characterisation, Testing and Simulation, Nanyang Technological University, Singapore, for use of their electron microscopy/X-ray facilities. H.S.N. acknowledges the financial support from the French National Research Agency (ANR) under the project POLAROID (ANR-24-CE24-7616-01).

REFERENCES

(1) Asano, T.; Ochi, Y.; Takahashi, Y.; Kishimoto, K.; Noda, S. Photonic Crystal Nanocavity with a Q Factor Exceeding Eleven Million. *Opt. Express* **2017**, *25* (3), 1769.

(2) Gangwar, R. K.; Pathak, A. K.; Kumar, S. Recent Progress in Photonic Crystal Devices and Their Applications: A Review. *Photonics* **2023**, *10* (11), 1199.

(3) von Neuman, J.; Wigner, E. Uber Merkwürdige Diskrete Eigenwerte. Uber Das Verhalten von Eigenwerten Bei Adiabatischen Prozessen. *Phys. Z.* **1929**, *30*, 467−470.

(4) Hsu, C. W.; Zhen, B.; Stone, A. D.; Joannopoulos, J. D.; Soljačić, M. Bound States in the Continuum. *Nat. Rev. Mater.* **2016**, *1* (9), 16048.

(5) Kodigala, A.; Lepetit, T.; Gu, Q.; Bahari, B.; Fainman, Y.; Kanté, B. Lasing Action from Photonic Bound States in Continuum. *Nature* **2017**, *541* (7636), 196−199.

(6) Ha, S. T.; Fu, Y. H.; Emani, N. K.; Pan, Z.; Bakker, R. M.; Paniagua-Domínguez, R.; Kuznetsov, A. I. Directional Lasing in Resonant Semiconductor Nanoantenna Arrays. *Nat. Nanotechnol.* **2018**, *13* (11), 1042−1047.

(7) Wu, M.; Ha, S. T.; Shendre, S.; Durmusoglu, E. G.; Koh, W.-K.; Abujetas, D. R.; Sánchez-Gil, J. A.; Paniagua-Domínguez, R.; Demir, H. V.; Kuznetsov, A. I. Room-Temperature Lasing in Colloidal Nanoplatelets via Mie-Resonant Bound States in the Continuum. *Nano Lett.* **2020**, *20* (8), 6005−6011.

(8) Mylnikov, V.; Ha, S. T.; Pan, Z.; Valuckas, V.; Paniagua-Domínguez, R.; Demir, H. V.; Kuznetsov, A. I. Lasing Action in Single Subwavelength Particles Supporting Supercavity Modes. *ACS Nano* **2020**, *14* (6), 7338−7346.

(9) Ha, S. T.; Li, Q.; Yang, J. K. W.; Demir, H. V.; Brongersma, M. L.; Kuznetsov, A. I. Optoelectronic Metadevices. *Science* **2024**, *386* (6725), No. eadm7442.

(10) Romano, S.; Zito, G.; Torino, S.; Calafiore, G.; Penzo, E.; Coppola, G.; Cabrini, S.; Rendina, I.; Mocella, V. Label-Free Sensing of Ultralow-Weight Molecules with All-Dielectric Metasurfaces Supporting Bound States in the Continuum. *Photon. Res.* **2018**, *6* (7), 726.

(11) Yesilkoy, F.; Arvelo, E. R.; Jahani, Y.; Liu, M.; Tittl, A.; Cevher, V.; Kivshar, Y.; Altug, H. Ultrasensitive Hyperspectral Imaging and Biodetection Enabled by Dielectric Metasurfaces. *Nat. Photonics* **2019**, *13* (6), 390−396.

(12) Zito, G.; Sanità, G.; Guilcapi Alulema, B.; Lara Yépez, S. N.; Lanzio, V.; Riminucci, F.; Cabrini, S.; Moccia, M.; Avitabile, C.; Lamberti, A.; Mocella, V.; Rendina, I.; Romano, S. Label-Free DNA Biosensing by Topological Light Confinement. *Nanophotonics* **2021**, *10* (17), 4279−4287.

(13) Ardizzone, V.; Riminucci, F.; Zanotti, S.; Gianfrate, A.; Efthymiou-Tsironi, M.; Suàrez-Forero, D. G.; Todisco, F.; De Giorgi, M.; Trypogeorgos, D.; Gigli, G.; Baldwin, K.; Pfeiffer, L.; Ballarini, D.; Nguyen, H. S.; Gerace, D.; Sanvitto, D. Polariton Bose−Einstein Condensate from a Bound State in the Continuum. *Nature* **2022**, *605* (7910), 447−452.

(14) Dang, N. H. M.; Zanotti, S.; Drouard, E.; Chevalier, C.; Trippé-Allard, G.; Amara, M.; Deleporte, E.; Ardizzone, V.; Sanvitto, D.; Andreani, L. C.; Seassal, C.; Gerace, D.; Nguyen, H. S. Realization of Polaritonic Topological Charge at Room Temperature Using Polariton Bound States in the Continuum from Perovskite Metasurface. *Adv. Opt. Mater.* **2022**, *10* (6), 2102386.

(15) Weber, T.; Kühner, L.; Sortino, L.; Ben Mhenni, A.; Wilson, N. P.; Kühne, J.; Finley, J. J.; Maier, S. A.; Tittl, A. Intrinsic Strong Light-Matter Coupling with Self-Hybridized Bound States in the Continuum in van Der Waals Metasurfaces. *Nat. Mater.* **2023**, *22* (8), 970−976.

(16) Do, T. T. H.; Nonahal, M.; Li, C.; Valuckas, V.; Tan, H. H.; Kuznetsov, A. I.; Nguyen, H. S.; Aharonovich, I.; Ha, S. T. Room-Temperature Strong Coupling in a Single-Photon Emitter-Metasurface System. *Nat. Commun.* **2024**, *15* (1), 2281.

(17) Wu, X.; Zhang, S.; Song, J.; Deng, X.; Du, W.; Zeng, X.; Zhang, Y.; Zhang, Z.; Chen, Y.; Wang, Y.; Jiang, C.; Zhong, Y.; Wu, B.; Zhu, Z.; Liang, Y.; Zhang, Q.; Xiong, Q.; Liu, X. Exciton Polariton Condensation from Bound States in the Continuum at Room Temperature. *Nat. Commun.* **2024**, *15* (1), 3345.

(18) Carletti, L.; Koshelev, K.; De Angelis, C.; Kivshar, Y. Giant Nonlinear Response at the Nanoscale Driven by Bound States in the Continuum. *Phys. Rev. Lett.* **2018**, *121* (3), 033903.

(19) Anthur, A. P.; Zhang, H.; Paniagua-Dominguez, R.; Kalashnikov, D. A.; Ha, S. T.; Maß, T. W. W.; Kuznetsov, A. I.; Krivitsky, L. Continuous Wave Second Harmonic Generation Enabled by Quasi-Bound-States in the Continuum on Gallium Phosphide Metasurfaces. *Nano Lett.* **2020**, *20* (12), 8745−8751.

(20) Koshelev, K.; Kruk, S.; Melik-Gaykazyan, E.; Choi, J.-H.; Bogdanov, A.; Park, H.-G.; Kivshar, Y. Subwavelength Dielectric Resonators for Nonlinear Nanophotonics. *Science* **2020**, *367* (6475), 288−292.

(21) Park, J.-S.; Li, C.; Kim, K.-H.; Tang, Y.; Murphey, C. G. E.; Teitsworth, T. S.; Kim, S.; Harutyunyan, H.; Cahoon, J. F. Optical Nonlinearity in Silicon Nanowires Enabled by Bound States in the Continuum. *ACS Nano* **2023**, *17* (12), 11729−11738.

(22) Friedrich, H.; Wintgen, D. Interfering Resonances and Bound States in the Continuum. *Phys. Rev. A: At., Mol., Opt. Phys.* **1985**, *32* (6), 3231−3242.

(23) Zhen, B.; Hsu, C. W.; Lu, L.; Stone, A. D.; Soljačić, M. Topological Nature of Optical Bound States in the Continuum. *Phys. Rev. Lett.* **2014**, *113* (25), 257401.

(24) Jin, J.; Yin, X.; Ni, L.; Soljačić, M.; Zhen, B.; Peng, C. Topologically Enabled Ultrahigh-Q Guided Resonances Robust to out-of-Plane Scattering. *Nature* **2019**, *574* (7779), 501−504.

(25) Kang, M.; Zhang, S.; Xiao, M.; Xu, H. Merging Bound States in the Continuum at Off-High Symmetry Points. *Phys. Rev. Lett.* **2021**, *126* (11), 117402.

(26) Hwang, M.-S.; Lee, H.-C.; Kim, K.-H.; Jeong, K.-Y.; Kwon, S.-H.; Koshelev, K.; Kivshar, Y.; Park, H.-G. Ultralow-Threshold Laser Using Super-Bound States in the Continuum. *Nat. Commun.* **2021**, *12* (1), 4135.

(27) Kang, M.; Mao, L.; Zhang, S.; Xiao, M.; Xu, H.; Chan, C. T. Merging Bound States in the Continuum by Harnessing Higher-Order Topological Charges. *Light Sci. Appl.* **2022**, *11*, 228.

(28) Le, N. D.; Bouteyre, P.; Kheir-Aldine, A.; Dubois, F.; Cueff, S.; Berguiga, L.; Letartre, X.; Viktorovitch, P.; Benyattou, T.; Nguyen, H. S. Super Bound States in the Continuum on a Photonic Flatband: Concept, Experimental Realization, and Optical Trapping Demonstration. *Phys. Rev. Lett.* **2024**, *132* (17), 173802.

https://doi.org/10.1021/acsnano.5c01972
ACS Nano 2025, 19, 19287−19296

(29) Baba, T. Slow Light in Photonic Crystals. *Nat. Photonics* **2008**, *2* (8), 465−473.
(30) Ek, S.; Lunnemann, P.; Chen, Y.; Semenova, E.; Yvind, K.; Mork, J. Slow-Light-Enhanced Gain in Active Photonic Crystal Waveguides. *Nat. Commun.* **2014**, *5* (1), 5039.
(31) Sakoda, K. *Optical Properties of Photonic Crystals*; Springer-Verlag, 2005.
(32) Leykam, D.; Flach, S. Perspective: Photonic Flatbands. *APL Photonics* **2018**, *3* (7), 070901.
(33) Tang, L.; Song, D.; Xia, S.; Xia, S.; Ma, J.; Yan, W.; Hu, Y.; Xu, J.; Leykam, D.; Chen, Z. Photonic Flat-Band Lattices and Unconventional Light Localization. *Nanophotonics* **2020**, *9* (5), 1161−1176.
(34) Dong, K.; Zhang, T.; Li, J.; Wang, Q.; Yang, F.; Rho, Y.; Wang, D.; Grigoropoulos, C. P.; Wu, J.; Yao, J. Flat Bands in Magic-Angle Bilayer Photonic Crystals at Small Twists. *Phys. Rev. Lett.* **2021**, *126* (22), 223601.
(35) Mao, X.-R.; Shao, Z.-K.; Luan, H.-Y.; Wang, S.-L.; Ma, R.-M. Magic-Angle Lasers in Nanostructured Moiré Superlattice. *Nat. Nanotechnol.* **2021**, *16* (10), 1099−1105.
(36) Nguyen, D. X.; Letartre, X.; Drouard, E.; Viktorovitch, P.; Nguyen, H. C.; Nguyen, H. S. Magic Configurations in Moiré Superlattice of Bilayer Photonic Crystals: Almost-Perfect Flatbands and Unconventional Localization. *Phys. Rev. Res.* **2022**, *4* (3), L032031.
(37) Kumar, A.; Tan, Y. J.; Navaratna, N.; Gupta, M.; Pitchappa, P.; Singh, R. Slow Light Topological Photonics with Counter-Propagating Waves and Its Active Control on a Chip. *Nat. Commun.* **2024**, *15* (1), 926.
(38) Vicencio, R. A.; Mejía-Cortés, C. Diffraction-Free Image Transmission in Kagome Photonic Lattices. *J. Opt.* **2014**, *16* (1), 015706.
(39) Huang, L.; Zhang, W.; Zhang, X. Moiré Quasibound States in the Continuum. *Phys. Rev. Lett.* **2022**, *128* (25), 253901.
(40) Hong, P.; Xu, L.; Ying, C.; Rahmani, M. Flatband Mode in Photonic Moiré Superlattice for Boosting Second-Harmonic Generation with Monolayer van Der Waals Crystals. *Opt. Lett.* **2022**, *47* (9), 2326.
(41) Harder, T. H.; Egorov, O. A.; Krause, C.; Beierlein, J.; Gagel, P.; Emmerling, M.; Schneider, C.; Peschel, U.; Höfling, S.; Klembt, S. Kagome Flatbands for Coherent Exciton-Polariton Lasing. *ACS Photonics* **2021**, *8* (11), 3193−3200.
(42) Luan, H.-Y.; Ouyang, Y.-H.; Zhao, Z.-W.; Mao, W.-Z.; Ma, R.-M. Reconfigurable Moiré Nanolaser Arrays with Phase Synchronization. *Nature* **2023**, *624* (7991), 282−288.
(43) Qin, H.; Chen, S.; Zhang, W.; Zhang, H.; Pan, R.; Li, J.; Shi, L.; Zi, J.; Zhang, X. Optical Moiré Bound States in the Continuum. *Nat. Commun.* **2024**, *15* (1), 9080.
(44) Delikanli, S.; Erdem, O.; Isik, F.; Dehghanpour Baruj, H.; Shabani, F.; Yagci, H. B.; Durmusoglu, E. G.; Demir, H. V. Ultrahigh Green and Red Optical Gain Cross Sections from Solutions of Colloidal Quantum Well Heterostructures. *J. Phys. Chem. Lett.* **2021**, *12* (9), 2177−2182.
(45) Nguyen, H. S.; Dubois, F.; Deschamps, T.; Cueff, S.; Pardon, A.; Leclercq, J.-L.; Seassal, C.; Letartre, X.; Viktorovitch, P. Symmetry Breaking in Photonic Crystals: On-Demand Dispersion from Flatband to Dirac Cones. *Phys. Rev. Lett.* **2018**, *120* (6), 066102.
(46) Munley, C.; Manna, A.; Sharp, D.; Choi, M.; Nguyen, H. A.; Cossairt, B. M.; Li, M.; Barnard, A. W.; Majumdar, A. Visible Wavelength Flatband in a Gallium Phosphide Metasurface. *ACS Photonics* **2023**, *10* (8), 2456−2460.
(47) Altintas, Y.; Gungor, K.; Gao, Y.; Sak, M.; Quliyeva, U.; Bappi, G.; Mutlugun, E.; Sargent, E. H.; Demir, H. V. Giant Alloyed Hot Injection Shells Enable Ultralow Optical Gain Threshold in Colloidal Quantum Wells. *ACS Nano* **2019**, *13* (9), 10662−10670.
(48) Du, W.; Wu, X.; Zhang, S.; Sui, X.; Jiang, C.; Zhu, Z.; Shang, Q.; Shi, J.; Yue, S.; Zhang, Q.; Zhang, J.; Liu, X. All Optical Switching through Anistropic Gain of $CsPbBr_3$ Single Crystal Microplatelet. *Nano Lett.* **2022**, *22* (10), 4049−4057.
(49) Mermet-Lyaudoz, R.; Symonds, C.; Berry, F.; Drouard, E.; Chevalier, C.; Trippé-Allard, G.; Deleporte, E.; Bellessa, J.; Seassal, C.; Nguyen, H. S. Taming Friedrich-Wintgen Interference in a Resonant Metasurface: Vortex Laser Emitting at an On-Demand Tilted Angle. *Nano Lett.* **2023**, *23* (10), 4152−4159.
(50) Hwang, M.-S.; Kim, H.-R.; Kim, J.; Yang, B.-J.; Kivshar, Y.; Park, H.-G. Vortex Nanolaser Based on a Photonic Disclination Cavity. *Nat. Photonics* **2024**, *18* (3), 286−293.
(51) Yang, J. K. W.; Berggren, K. K. Using High-Contrast Salty Development of Hydrogen Silsesquioxane for Sub-10-Nm Half-Pitch Lithography. *J. Vac. Sci. Technol. B* **2007**, *25* (6), 2025.
(52) Delikanli, S.; Isik, F.; Durmusoglu, E. G.; Erdem, O.; Shabani, F.; Canimkurbey, B.; Kumar, S.; Dehghanpour Baruj, H.; Demir, H. V. Observation of Optical Gain from Aqueous Quantum Well Heterostructures in Water. *Nanoscale* **2022**, *14* (40), 14895−14901.

https://doi.org/10.1021/acsnano.5c01972
ACS Nano 2025, 19, 19287−19296